Spatial solitons in semiconductor microcavities

L. Spinelli,[1] G. Tissoni,[1] M. Brambilla,[2] F. Prati,[3] and L. A. Lugiato[1]
[1]*INFM, Dipartimento di Fisica dell'Università di Milano, via Celoria 16, 20133 Milano, Italy*
[2]*INFM, Dipartimento Interateneo di Fisica del Politecnico di Bari, via E. Orabona 4, 7016 Bari, Italy*
[3]*INFM, Università di Milano, II Facoltà di Scienze, via Lucini 3, 22100 Como, Italy*
(Received 18 March 1998)

We consider a semiconductor microcavity driven by a coherent and stationary holding beam, in two distinct configurations. In the first, no carriers are injected in the multiple-quantum-well structure and the optical nonlinearity is governed by an excitonic resonance. The second corresponds to that of a vertical-cavity surface-emitting laser kept slightly below threshold. We describe both configurations using a unified model that includes both field diffraction and carrier diffusion. We calculate numerically both the time evolution and the stationary profile of the solitonic solutions, using a generalization of the radial integration technique introduced by Firth and Scroggie [Phys. Rev. Lett. **76**, 1623 (1996)]. We analyze the instability that forms spatial patterns and especially cavity spatial solitons. We predict the existence of these solitons in various parametric domains for both configurations. We demonstrate that these results are independent of the periodic boundary conditions used in the simulations. We show that, introducing a simple phase modulation in the holding beam, one can eliminate the motions of solitons that arise from noise and from amplitude gradients. The solitons are robust with respect to parametric variations, to carrier diffusion, and even to some amount of self-defocusing. This picture points to the possibility of realizing arrays of solitonic pixels using semiconductor microresonators. [S1050-2947(98)09909-0]

PACS number(s): 42.65.Sf, 42.65.Tg, 42.79.Ta

I. INTRODUCTION

Applications to information technology are one of the goals of the extensive work in the field of transverse pattern formation in nonlinear optical systems [1–6]. The main difficulty encountered is the fact that different points of an optical pattern are strongly correlated, so that any local modification introduced to encode information either strongly affects the whole pattern or is spontaneously erased. This problem can be solved by generating spatial structures that are individually addressable and independent from one another.

The idea is of considering the transverse planes, orthogonal to the propagation direction of the beam, as a blackboard on which light dots can be written and erased in any desired location. These spots are called spatial solitons (SSs). They are generated by shining localized address pulses in the system. The pulses locally create a bleached area that persists after the passage of the pulse, hence the name ''optical bullet holes'' also used for this kind of spatial soliton [7]. The bleached area exerts a guiding action on the optical field that counterbalances the diffractive spreading and thus makes the soliton structure self-sustaining. Such solitons can arise, as discussed in [7], in the absence of any refractive effect. The temporal solitons familiar from nonlinear fiber optics are due to self-focusing and we show that spatial solitons based on a refractive nonlinearity can also exist as stable structures in a optical cavity. In the general case, both refractive index and absorption (or gain) exhibit nonlinearity and we find spatial solitons also in such intermediate cases.

Though there is extensive literature on spatial solitons (see, e.g., [8,9]), the concepts developed in the past were based on beam propagation, which instead plays a marginal role in our case. The basic property of the SSs considered in our scheme is that once they have been created by an address pulse, they persist as stationary dots until they are wiped out by another suitable pulse. This behavior is ensured by the optical cavity, a distinctive feature of our research that is absent in previous studies on spatial optical solitons.

Spatial solitons in cavity systems were predicted by Rosanov and Khodova [10–12]; in that case they arise from a standard plane-wave bistability in combination with switching waves with zero velocity. A different kind of cavity SS was predicted by Tlidi, Mandel, and Lefever [13,14]; in this case the mechanism is a modulational instability (MI) in combination with the coexistence between a hexagonal branch of bifurcated solutions and a plane-wave solution; this represents, in the domain of optics, an example of the phenomenon of ''localized structures'' previously discovered in other fields [15,16]. In this paper we discuss this kind of SS. Cavity SSs of chaotic character have been also found in [17], but here we will consider only stationary SSs.

In two previous papers a simple two-level model for a saturable absorber was analyzed [7,18]. In [7] the existence of stable spatial solitons in the system was predicted and the possibility of defining preferred locations by introducing a spatial phase modulation in the driving field was shown. Maxima in the phase profile of the driving field act as equilibrium positions for the SSs, which move to these sites even when the address pulse is not accurately aimed. In [18], on the other hand, the formation and control of SSs as a function of the characteristics of the address pulse were analyzed and their interaction properties were studied. In particular, the possibility of erasing SSs individually was investigated; this scheme was later successfully applied by Schreiber *et al.* to wipe out SSs in an optoelectronic system (a liquid-crystal light valve) [19]. Spatial solitons have been observed recently using an organic material (aberchrome) [20].

The results of [7,18] pave the way to the realization of an optical memory array of individually addressable spatial soli-

tons, with 2^{N^2} coexisting states for an array of N^2 solitons (i.e., $N\times N$). However, we are basically interested in demonstrating the feasible generation and controlling techniques for SSs in materials interesting for application; hence we present a model specifically designed to describe the case in which the nonlinear medium is a semiconductor.

Precisely, we formulate and analyze a unified model for a semiconductor material in a resonant microcavity driven by a coherent plane-wave field in two different configurations. The first corresponds to the case where the material has no population inversion; in the following, we will refer to this as the case of a ''passive system.'' More precisely, the material is assumed to be a multiple quantum well (MQW) with an exciton nonlinearity that is modeled as a Lorentzian line. The second corresponds to the ''active'' case of population inversion induced by an injected current. The configuration is basically that of a driven broad-area vertical cavity surface-emitting laser (VCSEL) with the gain arising from free carriers; however, the values of the current are such that the VCSEL is below threshold in absence of the driving field.

The motivation for the choice of these two configurations is the following. In our scheme, SSs develop in the neighborhood of a spatial modulational instability that destabilizes a stationary solution, homogeneous in the transverse plane. According to our previous experience, this instability tends to appear under conditions such that the input-output curve of the homogeneous stationary solution is S shaped, or close to S shaped. This is the reason why we use an optical resonator (the feedback of the cavity mirrors ensures the possibility of bistable response), while the two configurations (passive and active) described above were selected because they readily lead to the S-shaped regime. Note, however, that the homogeneous stationary solution in the lowest branch of the S-shaped curve must actually be *stable* against small perturbations if stable SSs are to exist. In particular, this is the motivation for keeping the VCSEL below threshold. A further reason for considering these two configurations is that population inversion converts self-focusing media into self-defocusing media and vice versa; hence, in this way we have an important degree of freedom available.

Here we analyze in full detail the model previously introduced in [21]. It is formulated in such a way that it is as simple as possible, but incorporates all the main physical processes, e.g., carrier diffusion and the linewidth enhancement factor familiar in semiconductor lasers [22]. For simplicity, the model includes only one longitudinal mode of the cavity, which appears legitimate for the sort of microresonators considered here. The model takes on the form of a set of partial differential equations (PDEs), numerically integrated in space and time by means of split-step techniques.

It is well known that the numerical integration of this kind of PDE is a difficult matter that requires sophisticated procedures. For this reason we check the results of the complex and lengthy numerical integrations in time of the full model using a powerful technique recently developed in [7]. This numerical approach, called the shooting method, allows one to calculate the stationary SSs directly, bypassing dynamical transients. By assuming that SSs are cylindrically symmetric in the radial direction, it reduces the $(2+1)$-dimensional full problem to a one-dimensional problem. More importantly, because the method requires only the solution of ordinary differential equations, it can achieve very high spatial resolution.

Sections II and III are devoted to the detailed description of the semiconductor model and the analytical calculation of the homogeneous stationary solutions and their stability. In Sec. IV we report the features of the numerical split-step method we adopted for the integration of the model equations and we describe the results obtained in both the passive and the active case. We show also that the results on SSs are independent of the periodic boundary conditions used in the simulations and discuss effects that arise from the presence of either spatial modulation in the input field or noise. We describe also the formation of stripelike solitons under conditions such that SSs are not stable. In Sec. V we describe the shooting method and compare the results with those obtained via the split-step method. Section VI is devoted to a summary and discussion of the results.

II. MODEL

We consider a broad area semiconductor heterostructure in both the passive and the active configuration. The semiconductor microresonator is of the Fabry-Pérot type, with a MQW structure perpendicular to the direction z of propagation of the radiation inside the cavity. The total electric field is composed of a forward E_F and a backward E_B component

$$\mathcal{E}=\frac{1}{2}[E_F(x,y,z;t)e^{ik_z z}+E_B(x,y,z;t)e^{-ik_z z}]e^{-i\omega_0 t}+\text{c.c.}, \tag{1}$$

where $k_z=\omega_0 n/c$, with ω_0 being the frequency of the input field and n the background refractive index of the medium.

On the other hand, the material is described by the carrier density $\tilde{N}$. In the slowly varying envelope approximation the dynamical equations are

$$\frac{1}{2ik_z}\nabla_\perp^2 E_F+\frac{\partial E_F}{\partial z}+\frac{1}{v}\frac{\partial E_F}{\partial t}=\left(i\frac{\omega_0\Gamma}{2nc}\chi-\alpha_i\right)E_F, \tag{2a}$$

$$\frac{1}{2ik_z}\nabla_\perp^2 E_B-\frac{\partial E_B}{\partial z}+\frac{1}{v}\frac{\partial E_B}{\partial t}=\left(i\frac{\omega_0\Gamma}{2nc}\chi-\alpha_i\right)E_B, \tag{2b}$$

$$\frac{\partial\tilde{N}}{\partial t}=-\frac{\tilde{N}}{\tau_r}-B\tilde{N}^2+\frac{\epsilon_0}{2\hbar}\text{Im}(\chi)(|E_F|^2+|E_B|^2)+\frac{\tilde{I}}{eV_A}+\tilde{D}\nabla_\perp^2\tilde{N}. \tag{2c}$$

In these equations $v=c/n$; Γ is the confinement factor, which, in the case of a vertical cavity, is simply the ratio L_A/L of the length L_A of the region filled by the quantum wells (QWs) to the cavity length L; α_i is the linear absorption coefficient per unit length due to the material in the regions between the QWs and the mirrors; τ_r is the nonradiative recombination rate of carriers; B is the coefficient of radiative recombination involving two carriers; $\tilde{D}$ is the diffusion coefficient; $\tilde{I}$ is the intensity of the injected current (nonvanishing only in the active configuration); e is the electron charge; and V_A is the active volume. The transverse Laplacian

$$\nabla_\perp^2 = \frac{\partial^2}{\partial x^2} + \frac{\partial^2}{\partial y^2}, \tag{3}$$

where x and y are Cartesian coordinates orthogonal to z, describes diffraction in the paraxial approximation. The radiation-matter interaction is described by the linearized complex susceptibility [23,24]

$$\chi(\tilde{N}) = -\frac{nc}{\omega_0}\Theta A(\tilde{N}-\tilde{N}_0), \tag{4}$$

where $\tilde{N}_0$ is the transparency value of the carrier density and A is the differential absorption (gain) coefficient in the passive (active) case.

In the *passive configuration* $\Theta=(\Delta+i)/(1+\Delta^2)$ and $\Delta=(\omega_e-\omega_0)/\gamma_e$, where ω_e is the the central frequency of the excitonic absorption line, approximated by the Lorentzian shape [23], and γ_e is the half-width of the excitonic line. In the *active configuration* $\Theta=\alpha+i$ [24], where α is the linewidth enhancement factor [22].

We get rid of the longitudinal coordinate by applying the mean-field limit [25], which holds when the transmissivity T and the single-pass absorption/gain ($AL_A\tilde{N}_0$) are much smaller than unity. This is always true in a vertical cavity device and the ratio of these two quantities

$$C = \frac{AL_A\tilde{N}_0}{2T} \tag{5}$$

is called the bistability parameter. As it will become evident, it is equivalent to the parameter C of the two-level saturable absorber model used in [7,18]. In addition, one assumes that only one longitudinal cavity mode of frequency ω_c is relevant in the dynamics, due to the short cavity. In this limit it is possible to show that the two counterpropagating fields are approximately constant and equal along the cavity, so we set $F(x,y,t)=\overline{E_F}(x,y,z,t)=\overline{E_B}(x,y,z,t)$, where the overbar denotes the average over the longitudinal coordinate z; we also introduce the adimensional electric field

$$E = \sqrt{\frac{\epsilon_0 nc\tau_r A}{\hbar\omega_0}\mathrm{Im}(\Theta)}F. \tag{6}$$

Next, we take into account [24] the proper boundary conditions of the problem, with partially reflecting mirrors and an external field of frequency ω_0 and slowly varying envelope E_I injected into the cavity. In this way the cavity half-width $\kappa=vT/2L$ appears in the equation for the electric field as a damping term. Finally, we define the normalized carrier density $N=\tilde{N}/\tilde{N}_0$ and current $I=\tilde{I}/\tilde{I}_0$, where the transparency value of the injected current is given by $\tilde{I}_0=eV_A\tilde{N}_0/\tau_r$ (in the passive configuration I is equal to zero because no current is injected).

After these steps one arrives at the equations

$$\frac{\partial E}{\partial t} = -\kappa[(1+\eta+i\theta)E - E_I + 2Ci\Theta(N-1)E - ia\nabla_\perp^2 E], \tag{7a}$$

$$\frac{\partial N}{\partial t} = -\frac{1}{\tau_r}[N+\beta N^2 - I + |E|^2(N-1) - l_D^2\nabla_\perp^2 N], \tag{7b}$$

where $\eta=2\alpha_i L/T$, $\theta=(\omega_c-\omega_0)/\kappa$ is the cavity detuning parameter, $a=v/2\kappa k_z$ is the diffraction coefficient, $l_D=\sqrt{\tilde{D}\tau_r}$ is the diffusion length, and $\beta=B\tilde{N}_0\tau_r$.

The last step consists in passing to adimensional independent variables, by scaling time to the photon lifetime (κ^{-1}) and the transverse coordinates x and y to $\sqrt{a}$. The equations that will be the object of our following study are then

$$\frac{\partial E}{\partial t} = -(1+\eta+i\theta)E + E_I - 2Ci\Theta(N-1)E + i\nabla_\perp^2 E, \tag{8a}$$

$$\frac{\partial N}{\partial t} = -\gamma[N+\beta N^2 - I + |E|^2(N-1) - d\nabla_\perp^2 N], \tag{8b}$$

with the adimensional decay rate $\gamma=(\kappa\tau_r)^{-1}$ and diffusion coefficient $d=l_D^2/a$.

In order to perform an analysis as close as possible to the devices available nowadays, the choice of numerical values of the physical quantities characterizing our model was inspired by some experimental works on optical bistability in GaAs MQW structures (see, e.g., [26–28]) and on characterization of VCSELs (see, e.g., [29]). Typical values of physical parameters common to both configurations are

$$\lambda_0 \equiv 2\pi c/\omega_0 = 850 \text{ nm}, \quad n=3.5,$$
$$\tilde{N}_0 = 2\times10^{18} \text{ cm}^{-3}, \quad T=4\times10^{-3}, \quad L=2 \ \mu\text{m}. \tag{9}$$

With this choice of physical quantities, we are led to a cavity decay rate $\kappa=8.57\times10^{10}$ s^{-1} and to a diffraction coefficient $a=19.3\ \mu$m^2, for both configurations. These values imply that the time unit is $\kappa^{-1}=11.7$ ps and the space unit is $\sqrt{a}=4.39\ \mu$m. As for the other quantities, we have to consider the passive and the active configuration separately; realistic values are

$$L_A=300 \text{ nm}, \quad \tau_r=6 \text{ ns}, \quad l_D=2 \ \mu\text{m},$$
$$\alpha_i=2.5 \text{ cm}^{-1}, \quad B=1.3\times10^{-10} \text{ cm}^3 \text{ s}^{-1} \tag{10}$$

for the passive configuration and

$$L_A=50 \text{ nm}, \quad \tau_r=1 \text{ ns}, \quad l_D=1 \ \mu\text{m} \tag{11}$$

for the active configuration.

In the active case we neglect the additional absorption of the material and the radiative recombination of carriers (i.e., we set $\alpha_i=0$, $B=0$). In a broad-area device with a cross section $S\approx5000\ \mu$m^2 (for example, a square of about 70 $\times70\ \mu$m^2) the active volume V_A is about 250 μm^3, so that the transparency value of the injected current is $I_0=80$ mA (corresponding to a current density of $J_0=1.6$ kA/cm^2). The cavity detuning parameter θ can be chosen of order unity, corresponding to a mistuning $\Delta\lambda\approx1$ nm or less, between the driving wavelength λ_0 and the Fabry-Pérot resonance peak.

III. HOMOGENEOUS SOLUTION AND LINEAR STABILITY ANALYSIS

The homogeneous solution (E_S, N_S) of Eqs. (8a) and (8b) is obtained by setting equal to zero the time derivatives and neglecting the Laplacian in the two equations. We obtain

$$|E_I|^2 = |E_S|^2\{[1+\eta-2C\ \mathrm{Im}(\Theta)(N_S-1)]^2 + [\theta+2C\ \mathrm{Re}(\Theta)(N_S-1)]^2\}, \tag{12a}$$

$$N_S = -\frac{1+|E_S|^2}{2\beta} + \frac{\sqrt{(1+|E_S|^2)^2+4\beta(|E_S|^2+I)}}{2\beta}, \tag{12b}$$

For appropriate choices of the parameters the curve of $|E_S|$ as a function of $|E_I|$ is S shaped.

The linear stability of the homogeneous solution is analyzed by studying the response of the system to small fluctuations around the steady state. We set

$$\begin{bmatrix} \delta E(x,y;t) \\ \delta E^*(x,y;t) \\ \delta N(x,y;t) \end{bmatrix} = e^{[\lambda t + i(K_x x + K_y y)]} \begin{bmatrix} \delta E_0 \\ \delta E_0^* \\ \delta N_0 \end{bmatrix}, \tag{13}$$

assuming that the fluctuations grow (or decay) exponentially in time and that they are modulated with transverse wave vector (K_x, K_y). The set of equations obtained linearizing Eq. (8a), its complex conjugate, and Eq. (8b) around the homogeneous stationary solution (12a) and (12b), and introducing the ansatz (13) admits nontrivial solutions only if the eigenvalue λ satisfies the cubic equation

$$\lambda^3 + a_2\lambda^2 + a_1\lambda + a_0 = 0, \tag{14}$$

where the coefficients a_i $(i=0,1,2)$ depend on the system parameters η, β, γ, Θ, θ, d, C, I, and E_I and the modulus square K^2 of the transverse wave vector

$$a_2 = 2A_1 + \gamma(A_4 + dK^2), \tag{15a}$$

$$a_1 = A_1^2 + (A_2+K^2)^2 + \gamma[2A_1(A_4+dK^2) + A_3\ \mathrm{Im}(\Theta)], \tag{15b}$$

$$a_0 = \gamma\{[A_1^2+(A_2+K^2)^2](A_4+dK^2) - A_3[(A_2+K^2)\mathrm{Re}(\Theta) - A_1\ \mathrm{Im}(\Theta)]\}, \tag{15c}$$

with

$$A_1 = 1+\eta-2C\ \mathrm{Im}(\Theta)(N_S-1), \tag{16a}$$

$$A_2 = \theta+2C\ \mathrm{Re}(\Theta)(N_S-1), \tag{16b}$$

$$A_3 = 4C|E_S|^2(N_S-1), \tag{16c}$$

$$A_4 = 1+|E_S|^2+2\beta N_S. \tag{16d}$$

Equation (14) has usually one real and two complex conjugate roots. The two complex eigenvalues might in principle give rise to a Hopf instability, but a very simple argument shows that since $\gamma \ll 1$, the real part of the complex conjugate eigenvalues is always negative, so that there is no instability related to the complex eigenvalues. The instability associated with the real eigenvalue is called a Turing or stationary instability because it brings the system to a new stationary state, different from the homogeneous one. The system passes from the stable to the unstable domain when the real eigenvalue changes its sign from negative to positive. Therefore, the stability boundary is assigned by the condition $\lambda = 0$, which is in turn equivalent to $a_0 = 0$. The latter condition leads to the following cubic equation in K^2:

$$d(K^2)^3 + (A_4+2dA_2)(K^2)^2 + [d(A_1^2+A_2^2) + 2A_2A_4 - \mathrm{Re}(\Theta)A_3]K^2 + A_4(A_1^2+A_2^2) - A_3[\mathrm{Re}(\Theta)A_2 - \mathrm{Im}(\Theta)A_1] = 0. \tag{17}$$

We fix all the parameters except the homogeneous intensity $|E_S|^2$ or, equivalently, the input intensity $|E_I|^2$ and we find, for every value of $|E_S|^2$, the corresponding interval of unstable wave vectors. The Turing instability domain can then be drawn in the plane $(|E_S|, K)$, where we can determine the unstable portion of the homogeneous solution and the critical wave vector K_C, which first destabilizes the homogeneous solution [see Figs. 1(b), 3(b), 4(b), 5(b), 8(b), and 9(b)].

IV. NUMERICAL ANALYSIS

A. Method of integration

The dynamical equations were integrated numerically using a split-step method with periodic boundary conditions. This method consists in separating the algebraic and the Laplacian terms on the right-hand part of the equations; the algebraic term is integrated using a Runge-Kutta algorithm, while for the Laplacian operator a two-dimensional (2D) fast Fourier transform is adopted. This implies that the number of points for each side of the grid must be a power of 2 and we mostly assumed a 64×64 grid. In order to ensure proper stability and convergence of the algorithm, we chose a time step $\delta t \approx 10^{-2}$ and a space step δs varying from 0.3 to 0.6.

For the typical values of the recombination time τ_r and the cavity decay rate κ given in Sec. II the values of the parameter $\gamma = (\kappa\tau_r)^{-1}$ are of order 10^{-2}–10^{-3}. However, in our simulations we adopt a much larger (up to $\gamma = 1$) value for γ because we observed that the only effect of decreasing γ is to make the transient regime longer; the structure of the final pattern does not depend on γ_1 as expected, since Eq. (17) does not bear a dependency on time rates in determining the instabilities' character. After having substantiated this claim with careful sample simulations, we decided to reduce the CPU time requirements by adopting high values of γ in further runs.

The technique used to switch on a SS consists in superimposing to the homogeneous background of the input field $E_I^{(h)}$ (which we assume real and positive without loss of generality) a Gaussian pulse, centered at the point (x_0, y_0) where we want to create the spatial soliton [18]. The injected field is then

$$E_I(x,y;t) = E_I^{(h)} + he^{i\varphi}\ \exp\left[-\frac{(x-x_0)^2+(y-y_0)^2}{2\sigma^2}\right] f(t), \tag{18}$$

with

$$f(t)=\begin{cases}1, & 0\leq t\leq \overline{t}\\ 0, & t>\overline{t},\end{cases} \tag{19}$$

where h and φ are the amplitude and phase of the Gaussian beam, σ is its width, and $\overline{t}$ is the pulse duration. We set $\varphi=0$, which means that the Gaussian beam is in phase with the background. A similar procedure is used to erase an SS: To this aim we create a dark hole in the homogeneous intensity of the injected field by setting the phase of the Gaussian pulse to $\varphi=\pi$ [obviously, in this case the Gaussian amplitude h in Eq. (18) must not exceed $E_I^{(h)}$].

In order to investigate the effects on SSs that arise by using more realistic configurations of the input field, we performed numerical simulations also considering a background input field with a broad Gaussian profile rather than a simply homogeneous one. In this case we assume

$$E_I(x,y)=E_I^{(h)}\exp\left(-\frac{x^2+y^2}{2\Sigma^2}\right) \tag{20}$$

in the absence of a switching pulse.

The pinning effect exerted on solitons by a phase modulation of the input field [7] is simulated by considering in the transverse plane two orthogonal standing waves of amplitude ζ superimposed on the homogeneous background and out of phase with respect to the latter by $\pi/2$. Hence the input field takes the form

$$E_I(x,y)=E_I^{(h)}[1+i\epsilon(\cos kx+\cos ky)], \tag{21}$$

where $\epsilon=2\zeta/E_I^{(h)}$. Provided ϵ is sufficiently small, E_I acquires essentially only a phase modulation: In fact, at first order in ϵ,

$$E_I(x,y)\approx E_I^{(h)}\exp[i\epsilon(\cos kx+\cos ky)], \tag{22}$$

while the correction to the intensity is only of order ϵ^2.

The pinning effect can also be analyzed in connection with the contemporary presence of a Gaussian modulation in the amplitude of the injected field. From expressions (20) and (21) the natural choice for the input field in this case is

$$E_I(x,y)=E_I^{(h)}\left[\exp\left(-\frac{x^2+y^2}{2\Sigma^2}\right)+i\epsilon(\cos kx+\cos ky)\right]. \tag{23}$$

Finally, in order to verify the effect of noise on the SSs, we included in our model the noise due to the driving field E_I and the injected current I. Thus we introduced white-noise terms, in the form of Gaussian processes with zero mean and δ correlated in space and time, to both Eq. (8a) for the field E and Eq. (8b) for the carrier density N.

B. Passive configuration

In the following we will analyze three particular cases of the passive configuration, relative to a resonant ($\Delta=0$), focusing ($\Delta<0$), and defocusing ($\Delta>0$) medium. In all three cases we set $I=0$, $\eta=0.25$, $\beta=1.6$, and $d=0.2$. The values of these parameters are directly derived from the physical quantities listed at the end of Sec. II.

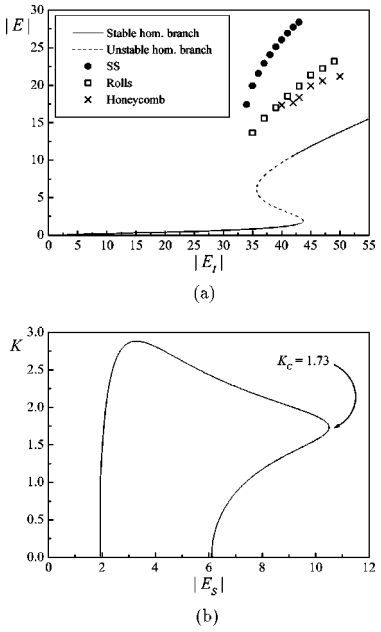

FIG. 1. Passive resonant case. (a) Steady-state curve of the homogeneous solution and results of numerical simulations. Different patterns are indicated by different symbols; the ordinate of the symbol corresponds to the maximum intensity in the pattern. (b) Turing instability domain. The parameters are $C=30$, $\theta=-3$, $\Delta=0$, $I=0$, $d=0.2$, $\eta=0.25$, and $\beta=1.6$.

1. Resonant case ($\Delta=0$)

The values for the remaining parameters are chosen $\theta=-3$ and $C=30$. The steady-state curve and the instability domain are shown in Fig. 1. In Fig. 1(a) we indicate with various symbols the results of numerical simulations when they produce some transverse pattern. The branch of SSs is represented by closed circles. Note that the SSs coexist with the lower branch of the homogeneous steady state. To the left of the stability domain the SSs are no longer stable because they progressively increase their radius while decreasing the peak intensity until they disappear. To the right of the stability domain new structures arise spontaneously and filaments appear, emerging from the background [see Fig. 2(a)]. Another situation that leads to the formation of filaments is when two SSs are excited too close to each other: In this case the structures repel each other and filaments are formed connecting the SSs. Filaments can be regarded as stripelike solitons and will be analyzed more extensively in Sec. IV F.

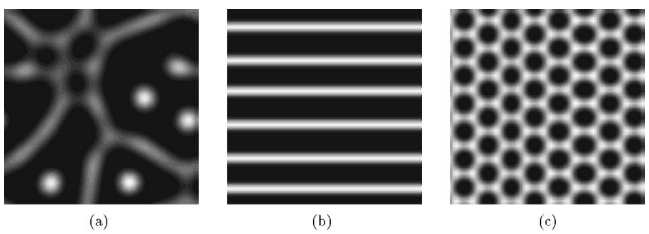

FIG. 2. Examples of patterns found in the passive resonant case (see Fig. 1). The three 2D gray scale plots (white represents the maximum of intensity) correspond to a square of 140×140 μm^2 in the cross-section of the beam: (a) dynamical coexistence of filaments and SS ($|E_I|=44$), (b) rolls ($|E_I|=39$), and (c) honeycomb ($|E_I|=48$).

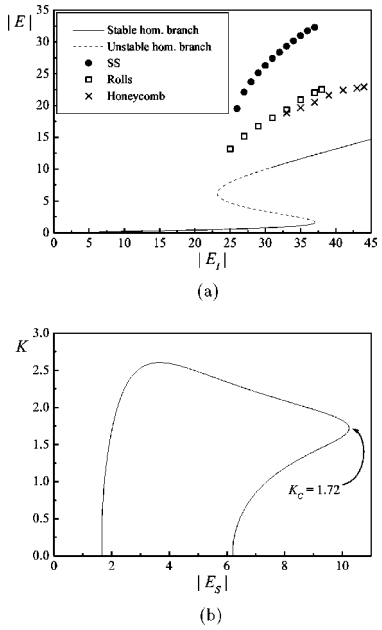

FIG. 3. Passive focusing case. (a) Steady-state curve of the homogeneous solution and results of numerical simulations. (b) Turing instability domain. The parameters are $C=40$, $\theta=-3$, $\Delta=-1$, $I=0$, $d=0.2$, $\eta=0.25$, and $\beta=1.6$.

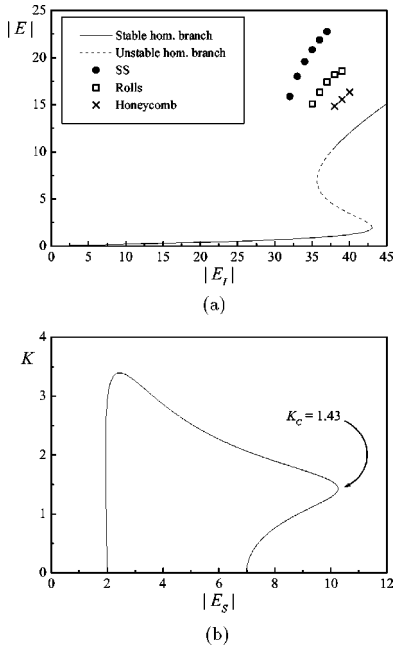

FIG. 4. Passive defocusing case. (a) Bistable steady-state curve of the homogeneous solution and results of numerical simulations. (b) Turing instability domain. The parameters are $C=40$, $\theta=-2$, $\Delta=1$, $I=0$, $d=0.2$, $\eta=0.25$, and $\beta=1.6$.

Other stable structures are the roll pattern [see Fig. 2(b)] and the honeycomb pattern [see Fig. 2(c)], represented in Fig. 1(a) by open squares and crosses, respectively. The picture is qualitatively very similar to the case of purely absorptive system, described in [30], the only relevant difference being that here we do not find stable positive hexagonal lattices for the parameter ranges examined in our simulations.

2. Focusing case ($\Delta<0$)

This is the situation where spatial solitons are most favored, since the focusing action of the medium cooperates with saturation to counteract diffraction. We consider in particular the case $\Delta=-1$, $\theta=-3$, and $C=40$. The steady-state curve with branches of different patterns and the instability domain are shown in Fig. 3.

An important feature of our device is the possibility of erasing a SS once it has been created. It can thus work as a memory, where a bit of information can be stored as well as wiped out. We have already mentioned at the beginning of this section which technique we use to erase an SS. In this particular case we checked the validity of this technique in two situations slightly different from the ideal one, namely, (a) when the center of the Gaussian beam is a bit displaced from the center of the SS and (b) when the Gaussian beam is not exactly in opposition of phase with respect to background. In both cases we fixed the amplitude and width of the Gaussian injected peak to $h=10$ and $\sigma=0.9$, respectively, while the background homogeneous input field is $E_I^{(h)}=27$ [see Eq. (18)]. Moreover, we set the darkening time around a typical value of $\bar{t}=300$, which corresponds to about 3.5 ns. Our simulations showed that in case (a) the SS can be erased when the separation between the Gaussian and the SS is smaller than 1.2 (5.27 μm), which approximately coincides with the size of a SS; for larger distances the SS simply moves a bit apart and decreases its peak intensity, but it survives. In case (b) we observe that, as expected, the best result is obtained at $\varphi=\pi$, but the SS can be erased quite fast for every value of φ between $2\pi/3$ and $4\pi/3$.

3. Defocusing case ($\Delta>0$)

This is a less favorable case for the formation of SSs because now both diffraction and self-defocusing act in the same direction. However, we were able to find several examples of robust SSs also in this situation. The parameters adopted for this case are $\Delta=1$, $\theta=-2$, and $C=40$ and $\Delta=1.5$, $\theta=-2$, and $C=20$. The steady-state curves and the stability domains are shown in Figs. 4 and 5, respectively. We note that in the first case the homogeneous steady-state curve shows bistability [Fig. 4(a)], while in the latter case the curve is monostable [Fig. 5(a)]. Branches of the various spatial patterns are also indicated with the usual symbols: The scenario is similar to what we obtained in the resonant and focusing case, with the only difference being that in the monostable case we found multistability among the lower branch of the homogeneous solution, SSs, and the hexagonal lattice, indicated by open triangles. This pattern is shown in Fig. 6, where the presence of several defects is evident.

From the Turing domain in Fig. 4(b) we find that the wave vector that destabilizes first the homogeneous solution is $K_C=1.43$, which corresponds to a critical wavelength $\lambda_C\equiv 2\pi/K_C=4.39$. On the other hand, from the measure of the cell length λ of the honeycomb pattern emerging at the instability threshold for $|E_I|=38$ we obtained $\lambda=4.56$: The two values λ and λ_C are in very good agreement.

Next we performed a detailed study of the behavior of the SSs when the integration parameters, i.e., the time step and the space step, are varied. In the bistable case ($\Delta=1$, $\theta=-2$, and $C=40$), we fixed the homogeneous input field at

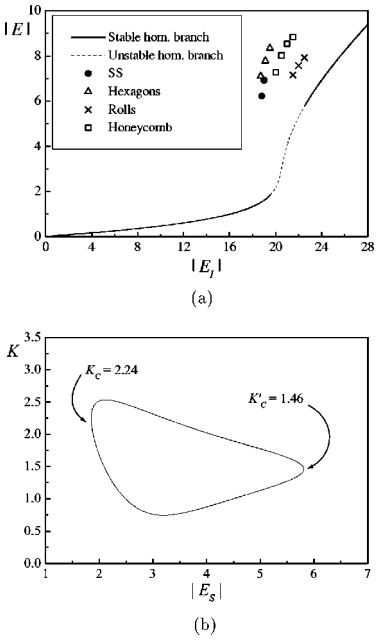

FIG. 5. Passive defocusing case. (a) Monostable steady-state curve of the homogeneous solution and results of numerical simulations. (b) Turing instability domain. Note the multistability among the lower homogeneous branch, SS, and hexagonal lattice. The parameters are $C=20$, $\theta=-2$, $\Delta=1.5$, $I=0$, $d=0.2$, $\eta=0.25$, and $\beta=1.6$.

$E_I^{(h)}=35$ and observed the changes in the peak intensity and in the diameter of the SS as the space step and the time step vary in a large range of values. We found that the SS persists for a space step as large as 0.8, when the typical value of its diameter is around 3. Moreover, the diameter and peak intensity vary little as the integration parameters are changed. These results indicate that the integration method is quite reliable.

In view of possible applications it is interesting to know what the minimum allowable distance is between two SSs because this is a measure of the density of information that can be stored in the system. Then we performed numerical simulations to investigate the interaction properties of SSs in the bistable case. We observed that two SSs of diameter 3.8 behave as distinct entities when their center-to-center distance is larger than 4.2, while they merge (i.e., they fuse into one soliton, with height, width, etc., identical to those of the two original solitons) as their distance goes below 3.6. In between, SSs repel each other until their distance reaches the noninteraction value 4.2. Obviously, these figures depend on the specific choice of the system parameters, but we can point out that this picture remains unchanged for the resonant and focusing cases and it is basically the same observed for a saturable absorber [18]. Moreover, we note that the interaction distance is very close to the critical length λ_C calculated above from the Turing domain. From this fact we can argue that the interaction properties of SSs are strictly related to the MI affecting the system. The merging and repulsion actions between two SSs can be seen as the way adopted by SSs to self-accommodate according to a underlying spatial pattern.

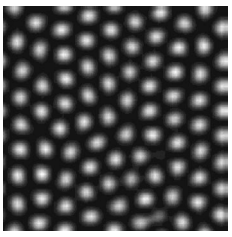

FIG. 6. Positive hexagonal pattern with defects found in the passive monostable defocusing case (see Fig. 5). The cross section is 169×169 μm^2 wide; $|E_I|=19.1$.

4. Variation of parameters

After seeing the three case studies, let us now discuss the key point of the parametric dependence of the results. The bistability parameter C must be large enough so that the input-output curve of the homogeneous stationary solution is bistable or close to bistable. The extension of the range of input intensities, for which SSs are found, becomes larger when C is increased. In our calculations, we varied C from 10 to 50; these values are accessible experimentally [26–28]. The parameter θ, which measures the detuning of the input frequency from the nearest longitudinal cavity mode in units of the cavity halfwidth, must be negative and typically $|\theta|$ must be on the order of 2 at least for the value of Δ considered in our calculations. As for the parameter Δ, for our choice of the parameters it results that in the self-defocusing case Δ must be about 2 or less; the existence of an upper limit in Δ is related to the fact that self-defocusing, which is unfavorable for SSs, increases with Δ. Our calculations performed after the publication of [21] have shown that, in the self-focusing case, also for $\Delta<-1$ it is possible to generate single SSs and not only groups of solitons.

As already discussed, the value of the ratio γ of the nonradiative recombination rate to the cavity damping rate turns out to be irrelevant. In a sense this is obvious because the solutions that correspond to SSs are stationary and γ governs only the transient stage. However, it must be kept in mind that γ may, *a priori*, influence strongly the stability of SSs, but in our calculations we found that a SS stable for $\gamma=0.1$ remains stable up to the realistic value $\gamma=0.002$.

As for the parameter β that governs radiative recombination, we considered two values, $\beta=0$ and 1.6. The picture is qualitatively the same in both cases; we saw only that, when $\beta=1.6$, the steady-state hysteresis cycle of the homogeneous stationary state corresponds to larger values of the input intensity, while SSs can resist to a stronger diffusion process (especially in the self-defocusing case).

The last parameter to be discussed is d, which governs the carrier diffusion. In Fig. 7 we show an example of Turing instability domains for different values of the diffusion coefficient d. We note that the instability domain shrinks as the diffusion parameter increases. Nevertheless, while the left boundary of the Turing domain is affected by diffusion, the right one is left almost unchanged by the increase of diffusion; both these features are positive for the existence of SSs in the presence of diffusion: In fact, the stability of the lower branch of the homogeneous solution together with an extended MI in the upper branch is a necessary condition for SSs to be stable. As a matter of fact, diffusion tends to stabilize the homogeneous solution. As for the effect of diffusion on SSs, we can note that when d is increased, the SS becomes lower and wider, and beyond a certain maximum

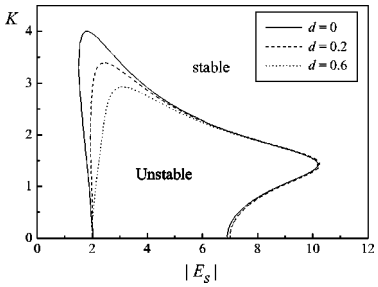

FIG. 7. Turing instability domains plotted for different values of d in the passive configuration. The other parameters are $C=40$, $\theta=-2$, $\Delta=1$, $I=0$, $\eta=0.25$, and $\beta=1.6$.

value d_{max} it does not exist anymore. In the self-focusing case diffusion is not at all a problem: We found stable SSs even when d was as large as 1.5 (typical values of d are on the order of 10^{-1}). For $\Delta=0$ it is basically the same and d can be safely raised to 0.75. As it may be expected, the self-defocusing case is more sensitive to the presence of diffusion. However, the robustness of SSs to carrier diffusion increases with their height and when this is large enough we found that d can be raised to 0.55 for $C\approx 20-40$, even in the presence of self-defocusing.

C. Active configuration

In this case the device is supplied by an injected current $\tilde{I}$ greater than the transparency value $\tilde{I}_0$ in such a way that $I>1$. In this configuration the microresonator becomes a vertical cavity surface-emitting amplifier or laser with an injected field E_I, according to whether or not the system is above laser threshold. In our study we always keep the system below lasing threshold in order to avoid the appearance of dynamical instabilities typical of the VCSEL above threshold.

In order to determine the threshold value I_{th} and the laser frequency in the absence of the injected field (the free-running regime) we must set $E_I=0$ in the stationary equations of the model and consider the point for which the nontrivial stationary solutions gives $|E_S|=0$. To this aim, we start from Eq. (12a). By setting $E_I=0$, dividing by $|E_S|^2$, and setting $\Theta=\alpha+i$ we obtain the two equations

$$1+\eta-2C(N_S-1)=0, \tag{24a}$$

$$\theta+2C\alpha(N_S-1)=0. \tag{24b}$$

On the other hand, from Eq. (12b) with $|E_S|=0$ and $I=I_{th}$ we obtain

$$N_S=\frac{-1+\sqrt{1+4\beta I_{th}}}{2\beta}. \tag{25}$$

From Eqs. (24a) and (24b) we obtain the condition that determines the laser frequency

$$\theta+\alpha(1+\eta)=0 \tag{26}$$

and the stationary carrier density at threshold

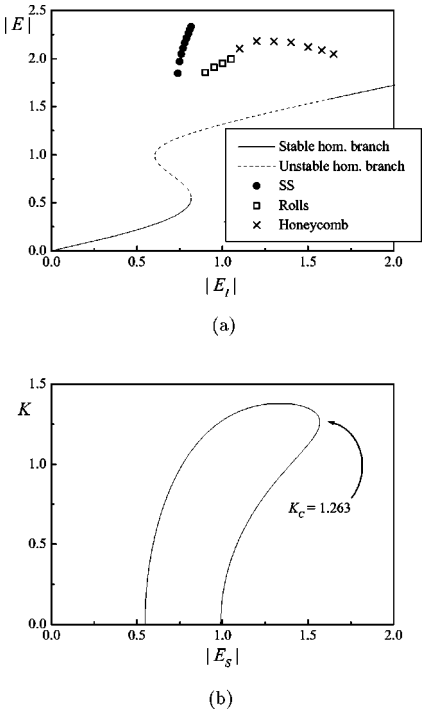

FIG. 8. Active focusing case. (a) Steady-state curve of the homogeneous solution and results of numerical simulations. (b) Turing instability domain. The parameters are $C=0.45$, $\theta=-2$, $\alpha=5$, $I=2$, $d=0.052$, $\eta=0$, and $\beta=0$.

$$N_S=1+\frac{1+\eta}{2C}, \tag{27}$$

which, by inserting Eq. (25), yields the condition for I_{th},

$$I_{th}=1+\frac{1+\eta}{2C}+\beta\left(1+\frac{1+\eta}{2C}\right)^2. \tag{28}$$

In the following we consider values $0<I<I_{th}$.

As we did in the passive configuration, we analyze the focusing ($\alpha>0$) and defocusing ($\alpha<0$) media separately. For the parameters of the active system, as in the passive case, we adopt numerical values derived from the physical quantities listed at the end of Sec. II. In particular, for a diffusion length $l_D=1\ \mu$m, the diffusion parameter d takes the value 0.052. Moreover, for the sake of simplicity, we neglect the linear absorption term and the quadratic recombination term choosing $\eta=0$ and $\beta=0$. In this case Eqs. (26) and (28) simplify, becoming $\theta=-\alpha$ and $I_{th}=1+1/2C$, respectively. As for the bistability parameter we fix $C=0.45$, leading to a threshold current $I_{th}=2.11$. We choose $I=2$ in order to keep the device just below threshold. We have also investigated the case in which the cross section of the active region is smaller than the integration window to verify the robustness of spatial solitons against the removal of periodic boundary conditions adopted to perform the numerical integration.

1. Focusing case ($\alpha>0$)

In this case we considered the parameters $\alpha=5$ and $\theta=-2$. In Fig. 8 we show the S-shaped curve of the homogeneous steady state and the Turing instability domain.

TABLE I. Minimum value of the amplitude h_{min} necessary to excite a SS, for different values of the lighting time $\overline{t}$ and of the width σ, [see Eq. (18)]. We set $E_I^{(h)}=0.75$ and $\varphi=0$.

σ	h_{min}
$\overline{t}=86$	
2	0.69
3	0.53
4	0.46
$\overline{t}=258$	
2	0.36
3	0.27
4	0.23

TABLE II. Minimum value of the amplitude h_{min} sufficient to annihilate the SS, for different choices of the width σ and of the darkening time $\overline{t}$ [see Eq. (18)]. We set $E_I^{(h)}=0.75$ and $\varphi=\pi$.

σ	h_{min}
$\overline{t}=8.6$	
2	0.40
3	0.34
4	0.31
$\overline{t}=25.8$	
2	0.21
3	0.17
4	0.16

Where the homogeneous solution is unstable, we found the stationary modulated patterns whose branches are indicated with the usual symbols.

We started our search just below the right-hand instability threshold. Here the system easily develops a perfect honeycomb pattern. Then we constructed the branch of the honeycomb pattern following its evolution for adiabatic variations of the input amplitude E_I. It turns out that the instability of the upper homogeneous solution is slightly subcritical: In fact, there is a superposition between a stable portion of the homogeneous curve and the honeycomb branch. By further decreasing the input amplitude E_I we observed the transition from the honeycomb pattern to rolls. We found both perfect and imperfect structures, depending on the initial conditions. For values of E_I just below the right-hand turning point of the S-shaped curve, we observed the presence of SSs. They are stable for E_I larger than about 0.74. Below this value, in fact, they disappear and the system evolves to the lower branch of the homogeneous stationary solution. Between the SSs and roll branches the system displays a dynamical behavior, in which we observed spontaneous creation and annihilation of spatial solitons and filaments in different locations of the transverse profile of the field and no stable configuration was found even for very long times.

Once we demonstrated the existence of a sizable branch of stable SSs, we studied the dependence of the switching and erasing procedures on the injection parameters, namely, the height h, the width σ, and the phase φ of the Gaussian beam superimposed on the homogeneous background and the lighting time $\overline{t}$. The amplitude of the homogeneous background in these simulations is $E_I^{(h)}=0.75$. First we set $\varphi=0$ and determined, for different values of the lighting time $\overline{t}$ and of the width σ, the minimum value of the amplitude h_{min} necessary to excite an SS [see Eq. (18)]. In Table I we summarized our results for two choices of the lighting time: $\overline{t}=86$ and 258 in unit κ^{-1}, which corresponds to 1 and 3 ns, respectively. Then we repeated the above simulations for the erasing case $\varphi=\pi$. We determined (see Table II) the minimum value h_{min} of the Gaussian amplitude sufficient to annihilate the SS for different choices of the width σ and of the darkening time $\overline{t}$. From our results it arises that for values h_{min} of the same order of magnitude, the darkening time necessary to switch off an SS is 10 times smaller than the lighting time for which the Gaussian pulse must be kept in order to switch on the SS. Moreover, we note that for the different values of σ considered, the value of h_{min} decreases by a factor 2 when $\overline{t}$ is increased by a factor 3.

Next we considered the switching problem when the phase φ of the Gaussian beam is not exactly equal to 0. We fixed $\sigma=3$ and a lighting time equal to 86 and then we determined, as before, the minimum amplitude h_{min} needed to excite a SS for various φ. The results are summarized in Table III. If we further increase the modulus of φ, that is, if we put the homogeneous background and the Gaussian pulse more and more out of phase, the process of exciting a SS becomes less and less efficient, up to the point that we are not able to switch on the SS: Heuristically, this can be understood by considering that when $|\varphi|$ becomes greater than $\pi/2$, we enter a regime where the Gaussian pulse acts to dig a dark spot in the homogeneous background rather than to create a peak of intensity. Nevertheless, Table III demon-

TABLE III. Minimum value of the amplitude h_{min} necessary to excite a SS, for different values of the phase φ [see Eq. (18)]. We set $E_I^{(h)}=0.75$, $\sigma=3$, and $\overline{t}=86$.

φ	h_{min}
$-\frac{\pi}{3}$	0.82
$-\frac{2}{9}\pi$	0.65
$-\frac{\pi}{9}$	0.56
$-\frac{\pi}{18}$	0.54
0	0.53
$\frac{\pi}{18}$	0.52
$\frac{\pi}{9}$	0.53
$\frac{2}{9}\pi$	0.57
$\frac{\pi}{3}$	0.67

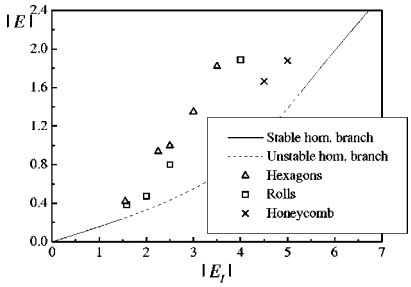

FIG. 9. Active defocusing case. (a) Steady-state curve of the homogeneous solution and results of numerical simulations. (b) Turing instability domain. The parameters are $C=0.45$, $\theta=-2$, $\alpha=-5$, $I=2$, $d=0.052$, $\eta=0$, and $\beta=0$.

strates that the choice of the phase φ is not critical: There is a wide range for φ (at least going from $-\pi/3$ to $\pi/3$) in which the excitation of a SS is reliable. Furthermore, we note a small difference in h_{min} for positive and negative φ. In particular, the excitation of a SS is more efficient if the Gaussian pulse is slightly dephased with respect to the homogeneous background: In fact, we found the minimum for the amplitude h_{min} when $\varphi=\pi/18$.

2. Defocusing case ($\alpha<0$)

As we did for the passive configuration, we have analyzed the defocusing case, even if it is unusual to have a negative linewidth enhancement factor in VCSELs. Nevertheless, we set $\alpha=-5$ and kept for the others parameter the values used in the focusing case. In particular, we note that in this case the homogeneous steady-state curve is monostable [Fig. 9(a)]. As a consequence, there are only modulational instabilities because the homogeneous solution is stable with respect to plane-wave perturbations [see Fig. 9(b)].

In Fig. 9(a) we show also the branches of the different spatial patterns. We note that the homogeneous solution is unstable for values of the input field $|E_I|$ between 1.53 and 5.28. In correspondence, a variety of spatial patterns develop. In contrast to the focusing case, we have the presence of a branch of positive hexagons (see Fig. 10). However, we did not find the formation of SSs: As a matter of fact, any attempt to excite a SS similarly to what we did for the focusing case was not successful. This is due to the fact that there is no coexistence between the hexagonal pattern and a stable portion of the homogeneous branch.

Then we measured the cell length of the patterns arising from the destabilization of the homogeneous solution at both extremes of the Turing instability and compared it with the characteristic length one would expect, given by the inverse

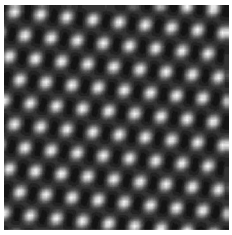

FIG. 10. Positive hexagonal pattern found in the active defocusing case (see Fig. 9). The cross section is 110×110 μm^2 wide; $|E_I|=1.55$.

of the critical wave vector K_C. For the hexagonal pattern in Fig. 10 corresponding to $|E_I|=1.55$ (the leftmost extremum of the Turing domain), we obtained a cell length of 2.94 against a critical length $\lambda_C\equiv2\pi/K_C=2.55$. Moreover, the honeycomb pattern arising at the other extremum of the Turing instability, when $|E_I|=5.25$, has a cell length of 4.70 to be compared with $\lambda'_C\equiv2\pi/K'_C=4.05$.

3. Variation of parameters

Here we briefly describe what happens when some of the main parameters of the model in the active configuration are changed, with particular attention to SSs. First, let us consider the variation of the diffusion parameter d. As in the passive case, an increase of diffusion reduces the portion of the homogeneous steady-state curve that is unstable against a modulated perturbation (see Fig. 11). However, the left boundary of the Turing domain is only slightly affected by diffusion and again this feature is positive for the existence of SSs in the presence of diffusion. The reduction of the unstable portion of the homogeneous solution has the consequence of shrinking and sometimes destroying the branches of the different spatial patterns in both the self-focusing and self-defocusing cases. Moreover, in the self-focusing case an increase of diffusion has practically no effect on the SS: The extension of the SS branch remains unperturbed even if the diffusion parameter d becomes as large as 1.

In the self-focusing case $\alpha>0$, we observed that a decrease in the bistability parameter C has greater consequences on the branch of SSs. In fact, the reduction of the bistable portion in the homogeneous steady-state curve, caused by the approaching of C to the bistability threshold, limits the extension of the input field region where the SSs exist. On the other hand, the features of the remaining spatial patterns result practically unchanged. Next we observed that also a decrease of the linewidth enhancement factor α from 5

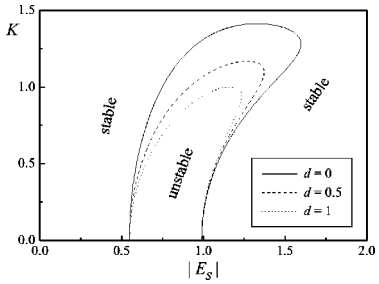

FIG. 11. Turing instability domains plotted for different values of d in the active configuration. The other parameters are $C=0.45$, $\theta=-2$, $\alpha=5$, $I=2$, $\eta=0$, and $\beta=0$.

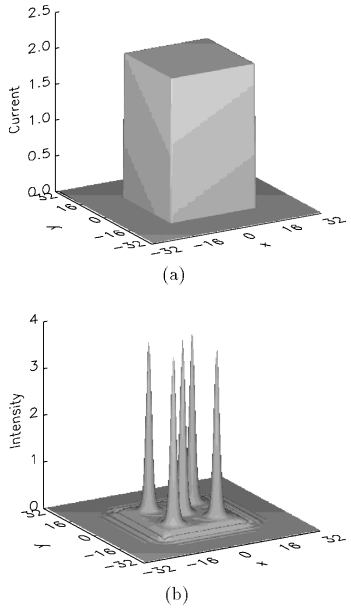

FIG. 12. Limited injected current. (a) Spatial profile of the current I. (b) Five stable SSs (3D plot). The parameters are the same as in Fig. 8. Spatial coordinates x and y are expressed in units of $\sqrt{a}$.

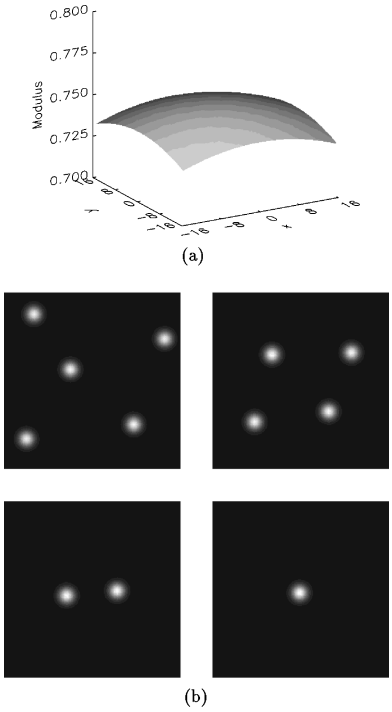

FIG. 13. Active focusing case. (a) Three-dimensional plot of the modulus of the driving field E_I with the Gaussian profile as given in Eq. (20): $E_I^{(h)}=0.75$ and $\Sigma=100$. Spatial coordinates x and y in (a) are expressed in units of $\sqrt{a}$. (b) Sequence of four frames describing the converging effect due to the Gaussian profile shown above. The time interval between two frames is 1296 (in units of κ^{-1}), while their cross section is 140×140 μm^2 wide. The other parameters are the same as in Fig. 8.

to about 3.5 leads to the disappearance of SSs. Nevertheless, this effect can be sometimes counteracted by a respective increment of $|\theta|$ (for example, SSs exist also for $\alpha=3.5$ and $\theta=-2.5$ at $|E_I|\approx0.128$).

The most important differences we met analyzing the self-defocusing case ($\alpha=-5$) with respect to the self-focusing one is the absence of stable spatial solitonic solutions and the appearance of the hexagonal pattern. Then we reverted the sign of the cavity-detuning parameter θ by fixing $\theta=2$, restoring in this way a bistable homogeneous steady-state curve. In general, in fact, one can observe that the homogeneous solution given by Eqs. (12a) and (12b) is symmetric with respect to the simultaneous change in sign of α and θ. In this case the MI is located in the lower branch of the bistable steady-state curve. From this instability we observed the supercritical bifurcation of stable hexagonal spatial patterns. Again, no stable SSs could be obtained.

4. Spatially confined injected current

Up to now, in our simulations, we have assumed that the injected current I, which pumps the microresonator in the active configuration, is homogeneous in the transverse plane. In actual devices, however, the active area has always a limited extension with a cross section that can take different shapes. It is important to include this feature in our model, in order to show that SSs are independent of the periodic boundary conditions used in the simulations. Furthermore, it is well known that boundaries strongly affect transverse spatial structures in different systems [31–33]. We are mainly interested in understanding whether boundary effects can affect SSs. It is worth noting that usually a limited profile in the driving field is assumed, while here we consider a limited profile in the pump current.

To this aim we considered a square active region with the size of the previous integration window for the active case, surrounded by a region without injected current, such that now the integration window has double the size. This was performed by increasing the number of grid points to 128×128. Outside the active region the system behaves like an absorber (i.e., there is no population inversion). The profile of the pump parameter I is shown in Fig. 12(a). We found that SSs are still stable also very close to the boundary of the active region; in Fig. 12(b) we give an example of five stable SSs. The suspicion that the SSs are an artifact of the numerical simulations, due to the imposition of periodic boundary conditions, is definitely eliminated.

D. Modulated driving field

Here we investigate, in both the passive and active configurations, what happens to SSs when the input field E_I is not homogeneous in the transverse plane but has some kind of spatial dependence. As anticipated in Sec. IV A, we analyzed first the effect of an injected field with a Gaussian profile. Figure 13(a) shows the input field with this kind of spatial modulation. In the passive case it turns out that the SSs are totally insensitive to intensity gradients, in the sense that SSs remain stable at locations where they have been created. In the active case, on the contrary, we observe a movement of SSs towards the maximum of the Gaussian profile. If we start with a certain number of SSs located in various points of the transverse plane, they begin to converge towards the center of the Gaussian profile, merging together when they are too close to remain independent. This process ends when there is only one SS located at the Gaussian peak.

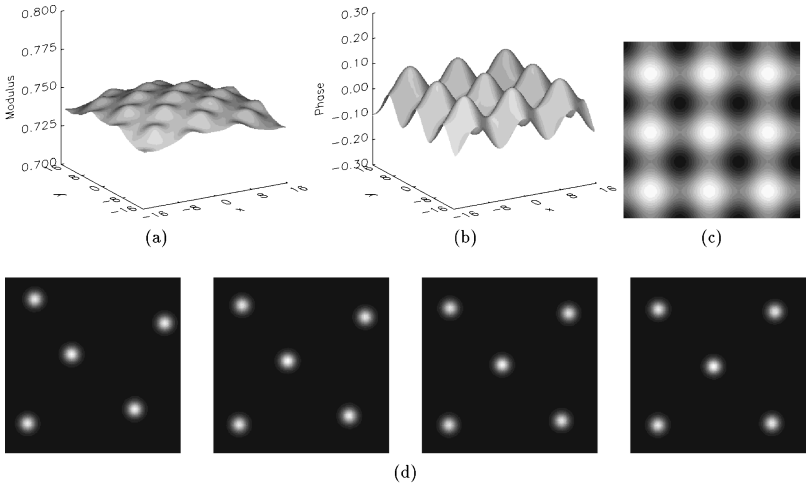

FIG. 14. Active focusing case. (a) Three-dimensional plot of the modulus of the driving field E_I with the Gaussian profile and phase modulation as given in Eq. (23): $E_I^{(h)}=0.75$, $\Sigma=100$, and $\epsilon=0.05$. (b) Three-dimensional plot of the phase of the driving field E_I. (c) Same as in (b), but in on a 2D gray scale plot. (d) Sequence of four frames showing the pinning effect due to the input field given above: The SSs move towards the maxima of the phase of E_I shown in (c). The time interval between two frames is 60 (in units of κ^{-1}), while the spatial coordinates x and y in (a) and (b) are expressed in units of $\sqrt{a}$. The cross section of the 2D plots in (c) and (d) is 140×140 μm^2 wide. The other parameters are the same as in Fig. 8.

In Fig. 13(b) we report a sequence of four frames to show this behavior: The numerical simulation begins with five SSs in different positions of the transverse plane and, after a suitable amount of time, only one SS remains in the center of the integration window (i.e., the center of the Gaussian profile). Obviously, this is an unwanted effect that can destroy any kind of information one would encode in the transverse plane by SSs.

We also studied the case of the phase modulation in the input field described in Sec. IV A. From [7], in fact, we know that a modulation in the phase of the injected field causes a drift of SSs towards the maxima of the function that describes the phase itself. This pinning effect is necessary in a soliton array memory to cancel possible errors in addressing solitons. As we expected, in both the passive and the active case a weak modulation produces a very fast drift of SS towards the nearest local maxima of the phase.

In the active case we analyzed the combined action of these two effects, that is, we consider the simultaneous presence of a Gaussian amplitude modulation, as before, and a phase modulation in the input field, as described in Eq. (23). We devoted particular attention to verify the possibility for the pinning action due to the phase modulation to be strong enough to overcome the converging effect of the Gaussian profile. We observed that it is possible, with a modulation amplitude $\epsilon=0.05$, to eliminate the converging motion caused by the input field as in Fig. 13(a). In Fig. 14(a) we report the profile of $|E_I|$ with both Gaussian and phase modulation, while in Figs. 14(b) and 14(c) the phase of E_I is reported in both 3D and 2D plots. Finally, in Fig. 14(d), four frames are shown describing the motion of SSs towards the maxima of the phase modulation even if a Gaussian curvature of the input field is present; the initial condition is the same we adopted in Fig. 13. Though from Fig. 14(a) it is evident that our choice of the phase modulation (see Sec. IV A) produces also a modulation in the intensity of E_I, the maxima of intensity are completely ignored by SSs in their motion.

E. Action of noise

We analyzed the behavior of SSs when some noise is present in our model. This is an important feature to study because in practical devices a more or less important amount of noise is always present; for this reason it is interesting to observe what happens to SSs in such a case.

We already know that we can excite a SS in any position of the transverse plane so that every point results marginally stable with respect to the presence of a SS. Due to this fact, one expects that the presence of noise causes a random walk of the SS in the transverse plane. Moreover, if the amount of noise becomes too large, one could also expect that an SS does not persist stably as an individual entity, but it is destroyed by random fluctuations.

To test these features, we inserted noise in our model, adding to the equations for the field E and the carrier density N white-noise terms. Precisely, we add to the right-hand side of Eqs. (8a) and (8b) two terms of the form $g_E\delta\xi_1(x,y;t)$ and $g_N\delta\xi_2(x,y;t)$, respectively, where $\delta\xi_i$ $(i=1,2)$ are Gaussian variables with zero mean and δ correlated in both space and time, while g_E and g_N measure the noise strength.

First, we performed a numerical simulation considering only the presence of noise and no spatial modulation in the input field. As we expected, SSs wander around until the distance between two of them becomes shorter than their interacting range, so that, eventually, the two merge together in a single SS. In Fig. 15 we show a sequence of frames taken at constant intervals during the time evolution, which shows the random walk experienced by the five SSs initially present (the initial condition is the same as in Fig. 13). In this simulation we set $g_E=g_N=0.03$. Note that, even in the presence of this quantity of noise, SSs are stable, apart from their interaction.

The random walk that SSs undergo can destroy any information encoded in the transverse plane by means of SSs, in the same way as the presence of a Gaussian profile in the driving field E_I does. As before, we thought to exploit the

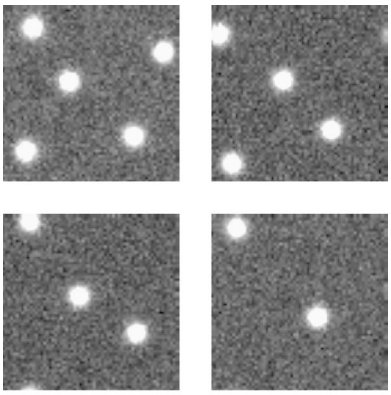

FIG. 15. Active focusing case. Sequence of four frames describing the random walk of SSs under the effect of noise, for a uniform input field; $g_E = g_N = 0.03$. The time interval between two frames is 7440 (in units of κ^{-1}), while their cross section is 140×140 μm^2 wide. The gray scale has been changed with respect to previous figures in order to emphasize the presence of noise. The other parameters are the same as in Fig. 8.

pinning effect exerted by the presence of a small phase modulation in the driving field in order to guide SSs towards the desired locations of the array.

To verify if this procedure is reliable, we carried out a numerical simulation with the same amount of noise as in Fig. 15, but this time with a slight phase modulation [$\epsilon = 0.05$ in Eq. (21)] added to the driving field. In Fig. 16 we show four frames taken at different times during the time evolution of the system. We can see that the added phase modulation is strong enough to overcome the random walk due to the noise and to pin down the SSs at the maxima of phase, arranging them in the positions of a 3×3 array. The only remaining effect of noise on SSs is a small random deformation of the peaks and a very short random displacement around their equilibrium positions.

F. Formation of stripelike solitons

The SSs described henceforth are two dimensional in the sense that they are self-confined in the (x,y) transverse plane. On the other hand, they can be regarded as zero-dimensional structures from the geometrical point of view because they can be assimilated to a single point in that plane, where they are completely defined by their location. In our simulations we encountered also what appear to be one-dimensional solitons in the sense that they are stripelike structures, each of which behaves independently; we will briefly report on them here since their behavior has not been thoroughly investigated yet.

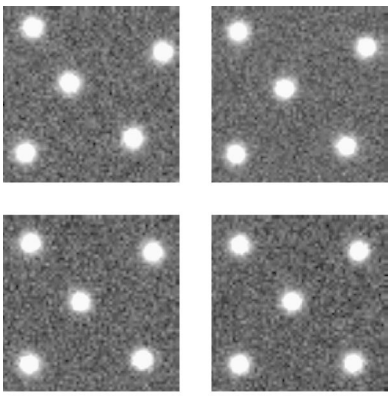

FIG. 16. Active focusing case. Sequence of four frames showing the pinning effect due to a driving field with a phase modulation in presence of noise; $\epsilon = 0.05$ and $g_E = g_N = 0.03$. The other parameters are the same as in Fig. 8. The time interval between two frames is 92 (in units of κ^{-1}), while their cross section is 140×140 μm^2 wide and the gray scale is the same as in Fig. 15.

FIG. 17. Passive defocusing case. Sequence of three frames showing the formation of stripelike solitons from three SSs. We set $|E_I| = 38$, while the other parameters are the same as in Fig. 4. The time interval between two frames is 16 (in units of κ^{-1}), while their cross section is 280×280 μm^2 wide.

As it appears in Fig. 4, there exists an interval of values for E_I where the honeycomb pattern coexists with the roll pattern and the SSs are not stable anymore. As one can intuitively expect, a competition between the two sorts of structures occurs, but it does not result in one overcoming the other; on the contrary, at the regime one meets a new scenario. Suppose that a single SS is excited in this interval by means of a beam pulse; at the regime one observes that the structure does not remain self-confined, but starts elongating and eventually becomes a wandering, writhing stripe whose length increases, while its width remains on the size of the soliton diameter. The initial orientation of the stripe is random, but can be controlled by a slight ovalization of the addressing pulse, the stripe emerging along the larger ellipse axis.

Elementary features of the interaction among stripelike structures have been evidenced by simulations; generally speaking, they tend to merge with each other whenever a collision between two stripe edges occurs, but it is also evident that adjacent stripes can mutually influence the local curvature radius. We could compare these results to previous, unpublished results concerning atomic saturable absorbers, where stripelike solitons had been observed; we infer that the carrier dynamics and possibly diffusion play a role in extending the stripe interaction range. This makes the control of the stripe location and curvature by means of external pulses more difficult. In Fig. 17 we report the evolution of three SSs created in the self-defocusing bistable case for $E_I = 38$. In Fig. 17(a) the initial condition of the simulation is shown: SSs are at a distance slightly larger than their interaction range (see Sec. IV B 3). The SSs start elongating as described above and become stripes that strongly interact and mutually merge [see Fig. 17(b)], giving rise to a complicated structure, reported in Fig. 17(c).

The character of the interaction is not univocal in the sense that two stripe fronts approaching each other can either merge or cause the deflection of the stripes and we have no evidence so far of a quantitative factor distinguishing between the two instances. Figure 18 shows the long-term evo-

FIG. 18. Passive defocusing case. Sequence of three frames showing the long-term evolution of the case described in Fig. 17. Again, $|E_I|=38$ and the other parameters are the same as in Fig. 4. The time interval between two frames is 16 (in units of κ^{-1}), while their cross section is 280×280 μm^2 wide.

lution of the previous case. Comparing Figs. 18(a) and 18(b), the front in the upper left quadrant has been deflected by the existing stripe towards the upper left corner. On the other side, a comparison between Figs. 18(b) and 18(c) shows that the front coming from the lower right corner, impinging on the lower part of the central structure, has collided and merged with it. All figures are separated by an interval of $t=16$ time units.

The question of whether these structures are stationary or restlessly dynamical is still under investigation. To our best comprehension it appears that the role of the boundaries is decisive in this respect: In our simulations, whenever a wandering stripe connects its two ends across the periodic boundary, it becomes stationary and particularly stable. In preliminary simulations with diffraction limited beams, we analyzed the behavior of the stripes in proximity of the injected field profile boundary. Although stripes stem from a competition with rolls, they do not connect orthogonally to the boundary [31]. Rather, they seem repelled thence and fold over to connect their ends in a figure that generally reflects the boundary symmetry and becomes stable. In Fig. 19(c) we plot the stationary pattern at the regime using a super-Gaussian (rather than plane-wave) holding beam, the

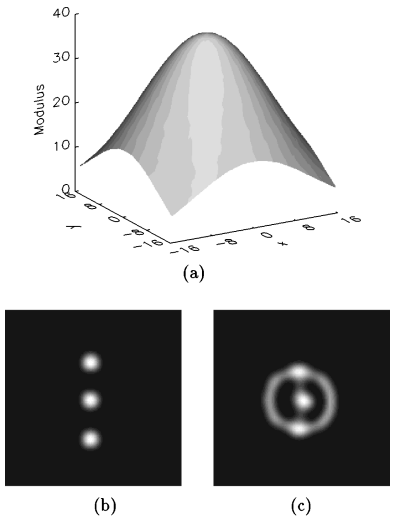

FIG. 19. Passive defocusing case. (a) Three-dimensional plot of the modulus of the driving field E_I with the super-Gaussian profile used for this numerical simulation. (b) Initial condition. (b) Stationary pattern of the regime. The width of the super-Gaussian profile is 99 μm, while the cross section of the two frames is 140×140 μm^2 wide. The parameters are the same as in Fig. 4.

profile of which is shown in Fig. 19(a); the initial condition with three SSs reported in Fig. 19(b) is the same used in Fig. 17, here magnified.

As for the interest associated with such structures, we can note that exactly as a line carries a higher semantic content, associated with its shape, length, local curvature, etc., these stripes may encode a larger information density, acting as elements of an alphabet. Of course, robust and unartifacted techniques must be designed to control them, a goal that lies beyond the scope of this paper.

V. SHOOTING METHOD

The radial integration method described in [7] can be successfully employed also in our model, in both the passive and active cases, to check the validity of the dynamical simulations. The idea is to find directly the radial stationary profile of SSs, bypassing the transient regime. This is done by performing a spatial integration of the stationary equations and assuming a cylindrically symmetric SS located at the center of the window. We describe here in details the technique adopted.

With respect to [7], here we have to cope with the major difficulty represented by the presence of one more equation for the carrier density N. For this reason we adopted a slightly different method in which the radial integration is performed outward from the origin and matching with the homogeneous solution is required at large r. This method has the advantage that it does not require us to express the trial solution as a combination of suitable Bessel functions as in [7] and therefore we do not need to calculate the eigenvalues of the coefficient matrix (which is now 3×3) of the linear system. We simply look for those initial values (at $r=0$) of the electric field $\overline{E}$ and carrier density $\overline{N}$ for which the solution integrated up to a fixed and large value r_1 of the radial coordinate is as close as possible to the homogeneous solution.

Let $(E(r;\overline{E},\overline{N}),(r;\overline{E},\overline{N}))$ be the solution obtained starting from the initial conditions

$$E(0)=\overline{E},\quad \frac{dE}{dr}(0)=0,$$
$$N(0)=\overline{N},\quad \frac{dN}{dr}(0)=0 \tag{29}$$

and (E_S,N_S) the homogeneous solution. We define the function

$$f(\overline{E},\overline{N})=\frac{1}{M}\sum_{m=0}^{M-1}[|E(r_1-m\Delta r;\overline{E},\overline{N})-E_S|^2 + |N(r_1-m\Delta r;\overline{E},\overline{N})-N_S|^2], \tag{30}$$

which measures the mean distance between the calculated solution and the homogeneous one, along the last M integration steps Δr. The problem now is that of finding the minima of f in the 3D space of the parameters $\overline{E}$ (complex) and N (real). For this reason the method is also called *shooting*, because one *shoots* starting from an initial condition in the

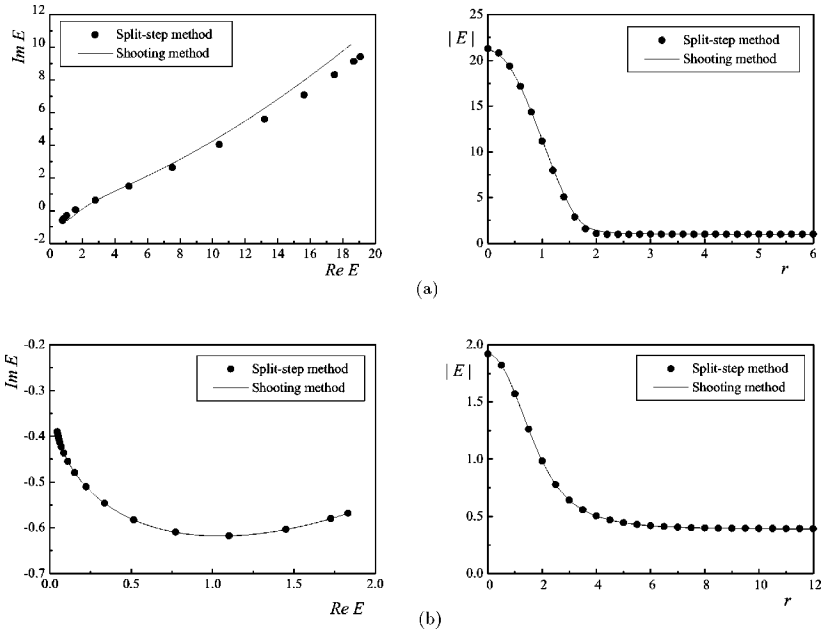

FIG. 20. Comparison between the radial integration (solid line) and the dynamical solution: (a) passive focusing configuration with the parameters set as $C=30$, $\theta=-3$, $\Delta=-1$, $I=0$, $d=0.2$, $\eta=0.25$, $\beta=1.6$, and $|E_I|=25$ and (b) active focusing configuration with the parameters set as $C=0.45$, $\theta=-2$, $\alpha=5$, $I=2$, $d=1$, $\eta=0$, $\beta=0$, and $|E_I|=0.75$.

3D space $(\overline{E},\overline{N})$ aiming at the particular points for which the function f is minimum. Usually we take M as one-tenth of the total number of steps; this ensures that f is small only for solutions that indeed tend to approach the homogeneous one, excluding those that accidentally cross the homogeneous at $r=r_1$. $E(r)$ and $N(r)$ are solutions of the stationary equations

$$E_I=(1+\eta+i\theta)E+2Ci\Theta(N-1)E-i\nabla_\perp^2 E, \tag{31a}$$

$$0=N+\beta N^2-I+|E|^2(N-1)-d\nabla_\perp^2 N, \tag{31b}$$

with the initial conditions (29). Therefore, one must integrate the set of ordinary differential equations

$$\frac{dE}{dr}=E_r, \tag{32a}$$

$$\frac{dE_r}{dr}=iE_I+[\theta-i(1+\eta)]E+2C\Theta(N-1)E-\frac{E_r}{r}, \tag{32b}$$

$$\frac{dN}{dr}=N_r, \tag{32c}$$

$$\frac{dN_r}{dr}=\frac{1}{d}[N+\beta N^2-I+|E|^2(N-1)]-\frac{N_r}{r} \tag{32d}$$

to calculate E and N at every r up to r_1 and then the function $f(\overline{E},\overline{N})$.

However, in almost all cases we found that the small diffusion parameter d in the denominator in Eq. (32d) makes the solution diverge before the point r_1 is reached. To circumvent this problem we adopted a perturbative method, in which we take advantage of the smallness of d to express N in a power series of d itself

$$N=N^{(0)}+dN^{(1)}+O(d^2). \tag{33}$$

By inserting this expansion into the stationary equations (31a) and (31b) and neglecting terms of order d^2 or higher, we find

$$N^{(0)}=[-(1+|E|^2)+\sqrt{\mathcal{A}}]/2\beta, \tag{34a}$$

$$N^{(1)}=2(4(I-1-\beta)[\mathrm{Re}(E_rE^*)]^2/\mathcal{A}-(N^{(0)}-1)\times\{[\theta+2C(N^{(0)}-1)\mathrm{Re}(\Theta)]|E|^2+E_I\,\mathrm{Im}(E)+|E_r|^2\})/\mathcal{A}, \tag{34b}$$

where $\mathcal{A}=(1+|E|^2)^2+4\beta(I+|E|^2)$. In this way, at every r, N is given to first order in d as a function of E and the set of equations reduces to

$$\frac{dE}{dr}=E_r, \tag{35a}$$

$$\frac{dE_r}{dr}=iE_I+[\theta-i(1+\eta)]E+2C\Theta E(N^{(0)}+dN^{(1)}-1)-\frac{E_r}{r}. \tag{35b}$$

Of course this approximate method is reliable only for small values of d, becoming exact for $d=0$; however, we found that it works well even for values of the diffusion coefficient d as large as 0.2, as shown in Fig. 20(a), where the results are compared with those of the split-step integration. For values of d as large as 1 the shooting method can be

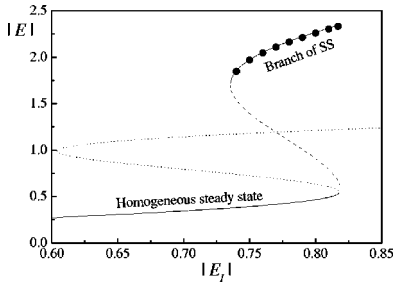

FIG. 21. Branch of SSs obtained by the shooting method in the perturbative approximation (solid line), valid for small d, compared with that derived by the split-step method (●), for the active case; the dashed line represents the unstable portion of the branch of SS (shooting method). The homogeneous solution is also shown. The parameters are the same as in Fig. 8.

applied without an approximation [see Fig. 20(b)]. The shooting method, in its perturbative form, has been exploited also to find branches of SSs. In Fig. 21 we reconstructed, by a radial integration of the stationary equations, the branch of SSs previously obtained by means of the split-step method [see Fig. 8(a)]: We note that the agreement between the results of two methods is very good. Furthermore, the shooting method allows us to construct also the unstable portion of the branch of SSs (the dashed line in Fig. 21), which cannot be determined via the split-step method. In this case $d=0.052$, so that the perturbative treatment of the carrier diffusion term is fully justified.

VI. CONCLUSIONS

We formulated and analyzed a model describing a semiconductor MQW vertical cavity in both the passive (no population inversion) and the active (VCSEL below threshold) cases. The numerical calculations were carried out by following two radically different approaches: (i) numerical integration in time and space of the partial differential equations and (ii) direct numerical calculation of the stationary SS profile, obtained by spatial integration of two ordinary differential equations. Whenever it was possible to use also the second approach, the results were in very good agreement with those of the time integration, which makes us fully confident that the data obtained from the first method are reliable in general.

Because the number of parameters in play is large and the same is true for the CPU time required by each simulation on PDEs, we could explore only rather limited but selected ranges of the parameters. These were suggested by our previous experience with modeling semiconductor optical systems and from experiments that are familiar to us; for example, the parametric values for the passive case were mainly suggested by experiments on excitonic optical bistability in GaAs MQWs, carried out by Sfez *et al.* in the past [26–28].

Despite this limitation, we were able to collect a significant set of numerical data, which led us to a clearcut picture for the appearance of SSs and their control. As a general rule, the region where one can readily find stable SSs corresponds to the leftmost extremum of the bifurcated branch arising from the modulational instability. This branch is shifted towards the left turning point of the bistable input-output curve of the homogeneous stationary solution or towards the inflection point when the curve is close to bistable. This rule of thumb applies equally well in the passive and active cases.

Also true in both cases is the following. (i) The parametric domains, where SSs exist, are sizably extended and accessible to the experimental realization. (ii) An increase of the parameter C (which is the bistability parameter) increases the extension of the interval of input field intensities where one meets stable SSs. (iii) SS are found for negative values of the cavity detuning parameter, i.e., the frequency of the relevant longitudinal cavity mode must be redshifted with respect to the frequency of the driving field. This does not hold in general, but is true when the detuning parameter Δ (in the passive case) or the linewidth enhancement factor (in the active case) is not large, as it is the case in our calculations in semiconductor systems. The requirement that θ be negative arises from the compensation between cavity detuning and the Laplacian contribution, described in [7,30] for the purely absorptive case. This compensation makes the cavity resonant with the field in correspondence to the solitonic peaks; for $\Delta \neq 0$, the resonance is with the cavity frequency shifted by the refractive index of the medium.

For the other parameters, let us discuss the two cases separately.

(i) Passive systems. We found stable SSs when the modulus of the detuning parameter Δ (which measures the detuning of the input frequency from the excitonic line, in units of the excitonic half-width) is on the order of or smaller than unity; i.e., one must operate in a neighborhood of the exciton resonance. The self-focusing case ($\Delta<0$) is in principle the most favorable for SS formation; in this case it is necessary to substantiate our results by further investigations based on a more complete model that includes also the free carrier continuum that lies on the self-focusing side of the exciton peak. Quite interesting and encouraging is that robust SSs have been found also in the case of self-defocusing material ($\Delta>0$), which is easiest to operate and for which our model should work best. The natural physical interpretation of this result is that the guiding effect provided by saturation [the guidance arising from the (negative) loss profile] is still able to overcome the antiguiding action of self-defocusing. Carrier diffusion is evidently also an effect that tends to damp SSs and represents an aspect that must be taken into account especially in the case of self-defocusing. However, the results indicate that for realistic values of the parameter d in Eq. (8b), carrier diffusion does not constitute a limitation in practice.

(ii) Active systems. Even though, as explained in the introduction, the VCSEL is kept below threshold, in order to obtain SSs the injected current must be such that the system is close enough to threshold (typically 5% below the lasing threshold). SSs were found when the linewidth enhancement factor is positive, which is the standard case. In our calculations we set $\alpha=5$; a drastic reduction of α leads to the disappearance of SSs, but this effect can be counteracted by increasing $|\theta|$. In recent experiments by Tredicce [34], which demonstrated the existence of standard optical bistability in VCSELs below threshold, the value of θ was small, but in order to obtain SSs it is necessary to increase $|\theta|$ to the order of some units. Carrier diffusion tends to limit the domain of

coexistence of SSs, but, since we are here in the context of a self-focusing system, it should not represent a problem. The analysis of the self-defocusing case, performed by setting $\alpha = -5$, led us to a variety of spatial patterns (roll, honeycomb, and hexagonal structures) with no appearance of SSs. With respect to the defocusing case in the passive configuration, this may be due to the value of the parameter α: $|\alpha| = 5$ against the value of detuning parameter $\Delta = 1$ in the passive case.

Furthermore, in order to make the modeling closer to real devices, we analyzed the effect induced by spatial modulation in the holding beam and in the pump current. The introduction of a Gaussian modulation in the amplitude profile of the holding beam causes different effects for the two configurations considered here: Precisely, in the passive case it seems not to affect SSs, which remain stable and unperturbed at their locations; on the contrary, in the active configuration SSs undergo a slow drift motion towards the point of the transverse plane where the maximum of the Gaussian profile of the input field is located. Therefore, starting with many SSs in different positions of the transverse plane, they merge all together and we are left with only one SS.

On the other hand, if we consider a spatial modulation in the phase of the holding beam, the behavior of SSs in the two configurations is the same: The SSs drift towards the closest local maximum of the phase. It is the same effect observed in a two-level saturable absorber [7] and it can be exploited to pin the SSs at precise positions in the transverse plane. We find that in the case of active configuration, the presence of both an amplitude Gaussian profile and a phase modulation in the holding beam causes a competition between the two and the result depends on the relative amplitudes of the two modulations. For appropriate choices of the two modulations, the pinning effect due to phase modulation overcomes the merging effect of the Gaussian profile of the holding beam and is also robust with respect to noise.

The consideration of a pump current with a limited cross section is very important in order to approach experimental realizations of this kind of devices. The persistence of SSs even in this environment is a significant signal of robustness of these structures. In fact, it means that SSs are completely independent of the periodic boundary conditions adopted in the integration.

In the paraxial approximation used in our models, the size of the SSs scales as $(\lambda \mathcal{L}/T)^{1/2}$, where λ is the wavelength, $\mathcal{L}$ is the length of the resonant cavity, and T is the transmissivity coefficient of the mirrors. In the case of standard microresonators, $\mathcal{L}$ is on the order of some wavelengths and T is very small, so that an increase in T would be beneficial to decrease the size of the SSs.

We analyzed also the process of writing and erasing SSs by means of narrow laser pulses; the picture remains basically that described in [18]. Here we want to give some examples of the real power and energy we must supply to semiconductor devices analyzed in this paper to excite an SS. From Eqs. (9)–(11) we can calculate the numerical value of the rescaling factor of the intracavity field F, indicated in Eq. (6). Nevertheless, the most relevant physical quantity is the energy flux w outside the cavity, which is related to the adimensional intracavity field E by the relation

$$w = w_0 \frac{|E|^2}{\mathrm{Im}(\Theta) C}, \tag{36}$$

where $w_0 = \hbar \omega_0 L_A \tilde{N}_0 / 4n\tau_r$ and takes the value 0.17 kW/cm^2 in both the passive and active cases. Let us consider the passive resonant case: The values of the physical powers are obviously dependent on the system parameters, especially on β. For this reason we chose to make our simulations with $\beta = 0$ and other parameters set as in Sec. IV B 1: It results that, in order to write a SS at $|E_I| = 25$, it is necessary to use a Gaussian pulse of the form (18) with $h = 29$, $\sigma = 0.9$, and $\overline{t} = 6$ ns. Correspondingly, we have a pulse power of 2.3 mW, which means a switching energy of 14 pJ, while the power of the holding beam, in the case of a cross section $S = 5000\ \mu$m^2, is 0.18 W. In the active case, from parameters established in Table I for the Gaussian pulse necessary to write a SS, we can calculate an addressing power of 0.12 mW (corresponding to 0.36 pJ switching energy) and a holding power (for a cross section $S = 5000\ \mu$m^2) of 11 mW. We note that the figures just stated are in reasonable agreement with the powers available and used in modern experiments with semiconductor devices that can be described by the model introduced in this paper. Further, we showed that a SS can be erased even when the address pulse is not aimed exactly, i.e., the system is able to self-accommodate some errors in the position of the address pulse with respect to that of the SS to be wiped out. The time scale is set by the slowest of the time constants in play that, in the case of semiconductors, correspond to the carrier recombination time τ_r.

The results of our theoretical and numerical calculations lead us to conclude that the realization of an array of spatial solitons using semiconductor materials is feasible. By appropriate selection of the operative conditions, both the active and passive cases present promising perspectives to reach this objective.

The formation of SSs in photorefractively pumped ring resonators [35] and in active cavities with a saturable absorber [36,37] has been reported. Also the possibility of having SSs with quadratic nonlinear media has been predicted recently [38,39].

After completion of the calculations reported in this paper, we were informed about an article of Michaelis, Peschel, and Lederer [40] that analyzes a numerical model identical to Eqs. (8a) and (8b) in the passive case, but without linear and nonlinear absorptive terms. The authors predict the formation of stable SSs under conditions of large detuning Δ, i.e., for strong self-defocusing. This result has been obtained for values of C substantially larger than those considered in our paper. Under conditions of large Δ the nonlinearity has a strongly antiguiding role; because both field diffraction and carrier diffusion have a spreading effect, the mechanism that forms these cavity solitons is quite different from the usual one that holds for standard SSs, i.e., the balance between a spreading mechanism and the confining effect of a nonlinearity. These points, as well as the connection with the results presented here, must be clarified and this is left for future work.

ACKNOWLEDGMENTS

We are indebted to Willie Firth for suggesting to us the perturbative procedure in the diffusion parameter d to adapt the shooting method to the model we analyzed. We are grateful to R. Kuszelewicz for several illuminating discussions on the choice of the parametric values in our calculation. This research was carried out in the framework of the ESPRIT Long Term Research Project PASS and the MURST Project Spatial Pattern Control in Sistemi Ottici Nonlineari.

[1] F. T. Arecchi, Physica D **51**, 450 (1991).
[2] L. A. Lugiato, Phys. Rep. **219**, 293 (1992).
[3] C. O. Weiss, Phys. Rep. **219**, 311 (1992).
[4] L. A. Lugiato, Chaos Solitons Fractals **4**, 1251 (1994).
[5] W. J. Firth, in *Self-Organization in Optical Systems and Applications in Information Technology*, edited by M. A. Vorontsov and W. B. Miller (Springer-Verlag, Berlin, 1995), p. 69.
[6] L. A. Lugiato, M. Brambilla, and A. Gatti, Adv. At. Mol. Opt. Phys. (to be published).
[7] W. J. Firth and A. J. Scroggie, Phys. Rev. Lett. **76**, 1623 (1996).
[8] P. V. Mamyshev, A. Villeneuve, G. I. Stegeman, and J. S. Aitchison, Electron. Lett. **30**, 726 (1994).
[9] B. Crosignani, M. Segev, D. Eugin, P. Di Porto, A. Yariv, and G. Salamo, J. Opt. Soc. Am. B **10**, 446 (1993).
[10] N. N. Rosanov and G. V. Khodova, Opt. Spectrosc. **65**, 449 (1988).
[11] N. N. Rosanov, J. Opt. Soc. Am. B **7**, 1057 (1990).
[12] N. N. Rosanov, in *Progress in Optics*, edited by E. Wolf (North-Holland, Amsterdam, 1996), Vol. XXXV.
[13] M. Tlidi, P. Mandel, and R. Lefever, Phys. Rev. Lett. **73**, 640 (1994).
[14] M. Tlidi and P. Mandel, Chaos Solitons Fractals **4**, 1475 (1994).
[15] O. Thual and S. Fauve, J. Phys.: Condens. Matter **49**, 1829 (1988).
[16] S. Rabinovich, J. Dewel, P. Borckmans, A. De Wit, B. Rudovics, J.-J. Perrand, E. Dulos, J. Boissonade, and P. De Kepper, Physica A **213**, 181 (1995).
[17] M. Le Berre, D. Leduc, S. Patrascu, E. Ressayre, and A. Tallet, Chaos Solitons Fractals, special issue on patterns in nonlinear optical systems, edited by R. Neubecker and T. Tschudi (1998).
[18] M. Brambilla, L. A. Lugiato, and M. Stefani, Europhys. Lett. **34**, 109 (1996); Chaos **6**, 368 (1996).
[19] A. Schreiber, B. Thüring, M. Kreuzer, and T. Tschudi, Opt. Commun. **136**, 415 (1997); Chaos Solitons Fractals, special issue on patterns in nonlinear optical systems, edited by R. Neubecker and T. Tschudi (1998).
[20] C. O. Weiss (unpublished).
[21] M. Brambilla, L. A. Lugiato, F. Prati, L. Spinelli, and W. J. Firth, Phys. Rev. Lett. **79**, 2042 (1997).
[22] C. H. Henry, IEEE J. Quantum Electron. **18**, 259 (1982).
[23] V. Pellegrini, F. Fuso, E. Arimondo, F. Castelli, L. A. Lugiato, G. P. Bava, and P. L. Debernardi, Phys. Rev. A **50**, 5219 (1994).
[24] F. Prati, A. Tesei, L. A. Lugiato, and R. J. Horowicz, Chaos Solitons Fractals **4**, 1637 (1994).
[25] R. Bonifacio and L. A. Lugiato, Lett. Nuovo Cimento **21**, 505 (1978).
[26] B. Sfez, J. L. Oudar, J. C. Michel, R. Kuszelewicz, and R. Azoulay, Appl. Phys. Lett. **57**, 324 (1990).
[27] B. Sfez, J. L. Oudar, J. C. Michel, R. Kuszelewicz, and R. Azoulay, Appl. Phys. Lett. **57**, 1849 (1990).
[28] B. Sfez, R. Kuszelewicz, and J. L. Oudar, Opt. Lett. **16**, 855 (1990).
[29] J. L. Jewell, J. P. Harbison, A. Scherer, Y. H. Lee, and L. T. Florez, IEEE J. Quantum Electron. **27**, 1332 (1991).
[30] W. J. Firth and A. J. Scroggie, Europhys. Lett. **26**, 521 (1994).
[31] P. Manneville, *Dissipative Structure and Weak Turbulence* (Academic, San Diego, 1990).
[32] G. L. Oppo, M. Brambilla, and L. A. Lugiato, Phys. Rev. A **49**, 2028 (1994); G. L. Oppo, M. Brambilla, D. Camesasca, A. Gatti, and L. A. Lugiato, J. Mod. Opt. **41**, 1151 (1994).
[33] F. Papoff, G. D'Alessandro, G. L. Oppo, and W. J. Firth, Phys. Rev. A **48**, 634 (1993).
[34] J. R. Tredicce (unpublished).
[35] M. Saffman, D. Montgomery, and D. Z. Anderson, Opt. Lett. **19**, 518 (1994).
[36] V. Yu. Bazhenov, V. B. Taranenko, and M. V. Vasnetsov, Proc. SPIE **1806**, 14 (1992).
[37] V. B. Taranenko, K. Staliunas, and C. O. Weiss, Phys. Rev. A **56**, 1582 (1997).
[38] K. Staliunas and V. J. Sanchez-Morcillo, Opt. Commun. **139**, 306 (1997).
[39] C. Etrich, U. Peschel, and F. Lederer, Phys. Rev. Lett. **79**, 2454 (1997).
[40] D. Michaelis, U. Peschel, and F. Lederer, Phys. Rev. A **56**, R3366 (1997).